


Please cite the Published Version

Regmi, YN , Roy, A, Goenaga, GA, McBride, JR, Rogers, BR, Zawodzinski, TA, Labbé, N and Chmely, SC (2017) Electrocatalytic Activity and Stability Enhancement through Preferential Deposition of Phosphide on Carbide. ChemCatChem, 9 (6). pp. 1054-1061. ISSN 1867-3880

DOI: <https://doi.org/10.1002/cctc.201601477>

Publisher: Wiley

Version: Accepted Version

Downloaded from: <https://e-space.mmu.ac.uk/624776/>

Usage rights:  In Copyright

Additional Information: This is an Author Accepted Manuscript of an article published in Chem-CatChem by Wiley.

Enquiries:

If you have questions about this document, contact openresearch@mmu.ac.uk. Please include the URL of the record in e-space. If you believe that your, or a third party's rights have been compromised through this document please see our Take Down policy (available from <https://www.mmu.ac.uk/library/using-the-library/policies-and-guidelines>)

Electrocatalytic Activity and Stability Enhancement through Preferential Deposition of Phosphide on Carbide

Yagya N. Regmi,^{*[a]} Asa Roy,^[b, c] Gabriel A. Goenaga,^[d] James R. McBride,^[e] Bridget. R. Rogers,^[f] Thomas A. Zawodzinski, Jr.,^[c, d] Nicole Labbé,^[a] and Stephen C. Chmely^{*[a]}

Phosphides and carbides are among the most promising families of materials based on earth-abundant elements for renewable energy conversion and storage technologies such as electrochemical water splitting, batteries, and capacitors. Nickel phosphide and molybdenum carbide in particular have been extensively investigated for electrochemical water splitting. However, a composite of the two compounds has not been explored. Here, we demonstrate preferential deposition of nickel phosphide on molybdenum carbide in the presence of carbon

by using a hydrothermal synthesis method. We employ the hydrogen evolution reaction in acid and base to analyze the catalytic activity of phosphide-deposited carbide. The composite material also shows superior electrochemical stability in comparison to unsupported phosphide. We anticipate that the enhanced electrochemical activity and stability of carbide deposited with phosphide will stimulate investigations into the preparation of other carbide–phosphide composite materials.

Introduction

Recent years have seen a tremendous surge in the development of materials based upon earth-abundant elements that can efficiently catalyze electrochemical water splitting. Cost-effective and scalable alternatives to Pt-, Ru-, and Ir-based catalysts are critical to generate H₂ in affordable and abundant quantities.^[1] Carbides and phosphides of early transition metals

are among the most promising noble-metal-free electrocatalysts and have been investigated for hydrogen evolution reaction (HER) and oxygen evolution reaction (OER) in acidic, basic, and neutral environments.^[2] The overpotentials required to generate the widely accepted benchmark activity of 10 mA cm⁻² have approached within 50 mV of Pt/C for HER and IrO₂ for OER.^[3] Strategies such as synthesis of polymorphs and crystalline species, engineering extremely small and dispersed carbide and phosphide particles to populate catalytically active sites on the surface, supporting or caging nanoparticles on high surface area substrates, and formation of composite materials including core–shell structures have led to the reduction in overpotentials and improved stabilities.^[4]

Nickel phosphide, molybdenum phosphide, and molybdenum carbide are among the most promising non-noble-metal-based electrocatalysts for water splitting. Although nickel carbide tends to be unstable under electrocatalytic conditions, a recent report by Fan et al. has indicated that the activity and stability of Ni₃C can be improved by encasing the carbide in graphene.^[5] Several strategies have been reported over the years for preparing bimetallic catalysts comprised of Ni and Mo, and these have been investigated for a variety of reactions.^[6] Ni₃Mo₃C showed improved activity over Mo₂C if used as an anode material in fuel cells, but nickel molybdenum carbides as hydrogen evolution catalysts with comparable activities to that of Mo₂C have not been reported.^[7] Bimetallic nickel molybdenum phosphide with comparable activity to that of either nickel or molybdenum phosphide as a water splitting catalyst has also not been reported to the best of our knowledge. Most of the successful strategies for Ni- and Mo-based bimetallic electrocatalysts have instead been invested in either forming composites or doping.^[8]

[a] Dr. Y. N. Regmi, Dr. N. Labbé, Dr. S. C. Chmely
Center for Renewable Carbon
University of Tennessee
Knoxville, Tennessee 37996 (USA)
E-mail: yregmi@utk.edu
schmely@utk.edu


[b] A. Roy
Bredesen Center for Interdisciplinary Research and Education
Knoxville, Tennessee 37996 (USA)

[c] A. Roy, Dr. T. A. Zawodzinski, Jr.
Oak Ridge National Laboratory
Oak Ridge, Tennessee, 37831 (USA)

[d] Dr. G. A. Goenaga, Dr. T. A. Zawodzinski, Jr.
Department of Chemical and Biomolecular Engineering
University of Tennessee
Knoxville, Tennessee 37996 (USA)

[e] Dr. J. R. McBride
Department of Chemistry and Vanderbilt Institute of Nanoscale Science and Engineering
Vanderbilt University
Nashville, Tennessee 37240 (USA)

[f] Dr. B. R. Rogers
Chemical and Biomolecular Engineering
Vanderbilt University
Nashville, TN 37235 (USA)

 Supporting information and the ORCID identification number(s) for the author(s) of this article can be found under <http://dx.doi.org/10.1002/cctc.201601477>.

Hexagonal molybdenum carbide in particular has been seen as an effective host system for doping and a superior catalyst support. Previously, Leonard and co-workers have reported that carbides show enhanced mass-normalized activities of Pt in comparison with carbon if used as catalyst supports, and molybdenum carbide had the highest enhancement in normalized electrocatalytic activities among the transition metal carbides investigated.^[9] Further, the same group demonstrated that the Fe₂N-type hexagonal structure (β -Mo₂C) is the most active HER catalyst among various molybdenum carbide crystal phases.^[10] Additionally, if hexagonal molybdenum carbide was templated on multiwalled carbon nanotubes (MWCNT), the electrocatalytic activity was significantly enhanced.^[11] Nanostructured hexagonal Fe₂P-type nickel phosphide (Ni₂P) has one of the lowest HER overpotentials among non-noble transition metal compounds.^[12] Nickel phosphide of various stoichiometries and crystal structures can be prepared by variation of the metal precursor and reaction conditions by using a facile hydrothermal synthesis method.^[13] Moreover, numerous reports detail the preparation of bimetallic alloys of nickel and molybdenum by using a hydrothermal synthesis method that employs metal salts as precursors.^[14] Wang and co-workers recently reported that molybdenum sulfide can be prepared on a molybdenum carbide surface by using a hydrothermal synthesis method without any significant changes in the structure of the carbide itself.^[15] The composite material also showed improved HER activity in comparison to the constituent carbide and sulfide. Ni₂P has been supported on various carbon structures and other high surface area substrates to enhance the activity and/or improve stability.^[16] However, to the best of our knowledge, a carbide-supported nickel phosphide composite material has not been reported.

We report the selective deposition of hexagonal Fe₂P-type nickel phosphide (Ni₂P) by using a hydrothermal synthesis method on hexagonal Fe₂N-type β -Mo₂C templated on MWCNT by the carbothermic reduction of MoO₃. A facile hydrothermal synthesis route was selected because of the ease of access to various phases and potential of scalability.^[13] The Ni₂P phase was selected based on the reported reproducible phase purity compared with other nickel phosphide phases.^[17] Additionally, it also possesses several low 2θ lattice planes that are within 3% lattice mismatch of the first four diffraction peaks in Fe₂N-type Mo₂C. To analyze and compare the electrocatalytic activities of the composite materials with the corresponding nickel phosphide and molybdenum carbide, we have used HER in acidic and alkaline electrolytes as the model reaction. We propose that the apparent preference in deposition on carbide instead of the ubiquitously available MWCNT surfaces is a result of the intermetallic interaction between the two metals under hydrothermal conditions and the analogous hexagonal crystal structures of the two constituent materials. We also attribute the enhancement in catalytic activity and stability of hydrothermally synthesized nickel phosphide to the interfacial sites resulting from the deposition of phosphide on carbide.

Results and Discussion

Synthesis and physical characterization

A modified hydrothermal route as reported by Deng et al. was used to prepare catalysts containing various ratios of Ni₂P to Mo₂C, hereafter referred to as Ni₂P@Mo₂C(molar ratio).^[13] The stated ratios are based on post-synthesis inductively coupled plasma optical emission spectroscopy (ICP-OES) measurements. Mo₂C was first prepared by slight modification of a previously reported carbothermic method.^[11] To achieve uniform distribution of carbide nanoparticles, the oxide–MWCNT mixture was ball-milled for 24 h at 300 rpm prior to carbothermic reduction to obtain a more homogenous precursor powder. As excess red phosphorus is necessary to drive the reaction towards the product, all composite catalysts were annealed under an argon flow after hydrothermal incubation and purification to remove any unreacted phosphorus. Although phosphorus loss was observed at the annealing temperatures used here, TEM images of the phosphides and composites reveal copious amounts of phosphorus post annealing. As phosphorus contains several allotropes with a wide range of boiling points extending well above 500 °C, the observed phosphorus layers must be composed of allotropes with boiling points above 500 °C.^[18] Additionally, a 5% H₂ mixture in Ar was also employed to investigate the effects of annealing under reducing environments on catalytic activities.

Based on Scherrer analysis, as-synthesized Ni₂P@Mo₂C contains Ni₂P with crystallite size around 10 nm and Mo₂C with around 20 nm, as demonstrated by the diffraction patterns in Figure 1 a. On annealing under an argon flow at 500 °C for 12 h, Ni₂P crystallites grow dramatically to about 50 nm whereas Mo₂C crystallites remain unchanged, as demonstrated in Figure 1 b. Thus, molybdenum carbide remains structurally unaffected during the hydrothermal incubation and annealing. Among the lattice planes corresponding to the first four low 2θ diffraction peaks for Mo₂C, only the 002 plane ($D=2.364$ Å) does not have a corresponding lattice plane in Ni₂P that is within 5% of the lattice mismatch (Figure S1 in the Supporting

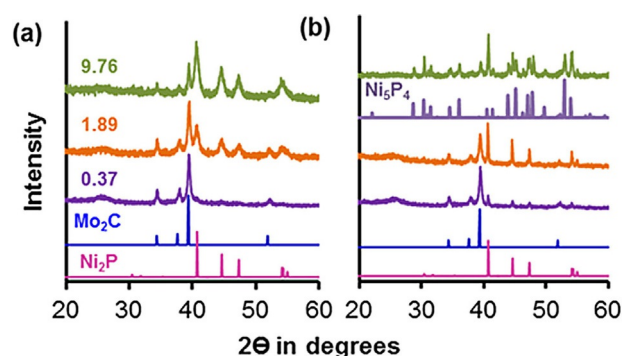


Figure 1. PXRD diffractograms of (a) the as-prepared nickel phosphide deposited on molybdenum carbide in the stated molar Ni₂P/Mo₂C determined by ICP-OES measurements. (b) Phosphide-deposited carbides annealed in an argon atmosphere at 500 °C for 12 h. The Ni₅P₄ PDF number is (00-018-0883).

Information). More significantly, the lattice plane corresponding to the most prominent diffraction peak (011) in Mo_2C with a d-spacing of 2.275 Å shows only a very low mismatch (2.68%) with the most intense diffraction peak (111) in Ni_2P . The 010 and 012 lattice planes in Mo_2C are also around 3% lattice mismatch with 020 and 030 lattice planes, respectively, in Ni_2P . Such a high degree of lattice alignments allows for the selective deposition of phosphide on carbide upon hydrothermal synthesis of Ni_2P in the presence of Mo_2C .

Further analysis suggests that phosphide preferentially deposits on carbide instead of unreacted MWCNT until the carbide surface saturates with phosphide. As demonstrated in Figure 1a, all as-synthesized $\text{Ni}_2\text{P}@/\text{Mo}_2\text{C}$ catalysts contain only Mo_2C and Ni_2P , irrespective of the phosphide-to-carbide (P/C) ratio. Upon annealing, at lower P/C ratios, only one phase of phosphide (Ni_2P) is observed, as apparent from Figure 1b. However, if the P/C ratio exceeds 1.89, a second nickel phosphide phase (Ni_3P_4) appears. Unsupported nickel phosphide and that supported on MWCNT also contain Ni_3P_4 at annealing under an Ar flow. Apparently, the carbide surface is saturated with phosphide around 1.89 P/C molar ratio, and any additional phosphide is either not directly interacting with the carbide surface or is depositing on the ubiquitously available carbon surface.

The carbide–phosphide interaction is critical to maintain monophasic nickel phosphide during annealing, and emergence of a second phase indicates saturation of the carbide surface with phosphide. Thus, a P/C ratio of 1.89 is referred to as the optimum molar ratio hereafter. XRD diffractograms for all the composite catalysts investigated here do not indicate the formation of possible impurities, that is, crystalline monometallic compounds nickel carbide, molybdenum phosphide, and the bimetallic nickel molybdenum carbide.^[5,6,19] The annealing temperatures employed here are below the formation temperatures reported for carbides and hydrothermal incubation of nickel chloride in the presence of Mo_2C does not indicate the presence of crystalline phosphides.^[9]

High-resolution (HR)-STEM micrographs, high angle annular dark field (HAADF) images, and energy-dispersive X-ray (EDX) maps in Figure 2b–e support the conclusion that the phosphide nanoparticles preferentially deposit on carbide nanoparticles. The most intense regions of Mo and Ni in Figure 2c,d correspond to the bright areas in the HAADF image in Figure 2b, indicating that the two transition metals are spatially co-localized. The overlap between Ni (Figure 2d) and P (Figure 2e) corroborates the XRD evidence in Figure 1 for formation of nickel phosphide instead of metallic nickel nanoparticles deposited on carbide. Additionally, composite catalysts are dispersed in a network of MWCNT (inset, Figure 2a). Prior to annealing, spherical phosphide particles around 10 nm are deposited on bigger carbide particles. The apparent composite particle size in Figure 2b is around 50 nm, which closely matches the estimation using Scherrer equation.

Catalyst surfaces were probed by using X-ray photoelectron spectroscopy (Figure 3). The high-resolution Mo3d spectrum in Figure 3a is analogous to the Mo_2C surface described previously for carbothermic reduction derived Mo_2C .^[11,20] Porosoff et al.

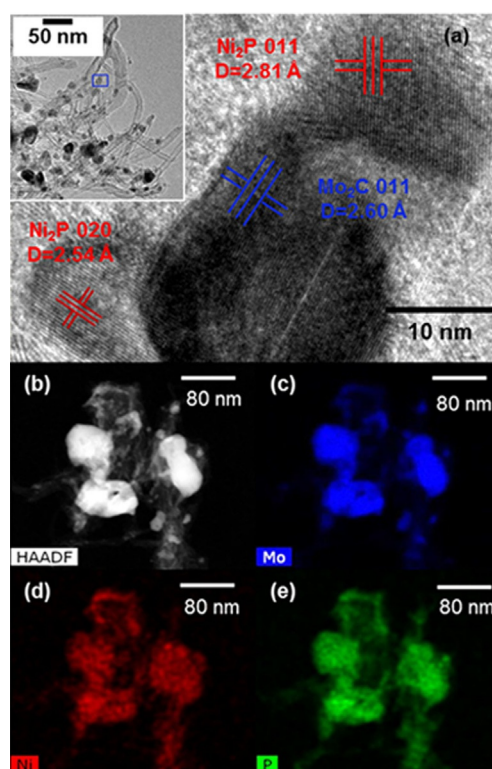


Figure 2. (a) High-resolution scanning transmission electron micrograph (HR-TEM) of as synthesized $\text{Ni}_2\text{P}@/\text{Mo}_2\text{C}$. Inset is the larger area TEM image with the area corresponding to the HR-STEM image marked in the blue rectangle. (b) High-angle annular dark field (HAADF) image of the annealed $\text{Ni}_2\text{P}@/\text{Mo}_2\text{C}$ with ICP-OES measured molar $\text{Ni}_2\text{P}/\text{Mo}_2\text{C} = 0.37$. Corresponding energy dispersive X-ray spectroscopy (EDX) elemental maps for (b) molybdenum, (c) nickel, and (d) phosphorus.

demonstrated that carbides have partially oxidized surfaces, and the degree of oxidation fluctuates during the course of a reaction cycle.^[21] The 2p spectrum for Ni from Ni_xP_y in Figure 3b indicates the presence of phosphided and oxidized nickel in addition to the broad satellite structures at higher binding energies.^[22] Similarly, the 2p spectrum corresponding to P from Ni_xP_y in Figure 3c reveals peaks that have previously been assigned as nickel phosphide and nickel phosphate.^[23]

The Mo3d spectrum for the composite material in Figure 3d indicates an increase in the relative intensity of peaks at lower binding energies compared with Mo_2C in Figure 3a. There is also a shift of about 0.5 eV to higher binding energies for all peaks for the composite material in comparison to Mo_2C (Table S1 in the Supporting Information). The Ni2p spectra from the composite in Figure 3e indicates formation of only oxidized nickel species and the P2p spectra in Figure 3f reveals the formation of P_2O_5 .^[23a,24] The relative growth of lower binding energy peaks indicates an increase in the metallic nature of the surface in the composite material with respect to Mo_2C .^[25] The increase in binding energy for the 3d peaks has previously been attributed to the increased intermetallic interaction between the transition metals.^[23a,26] Thus, the higher binding energy shift suggests an intermetallic interaction between Mo from Mo_2C and Ni from Ni_2P that was hydrothermally deposited on Mo_2C . Formation of phosphate

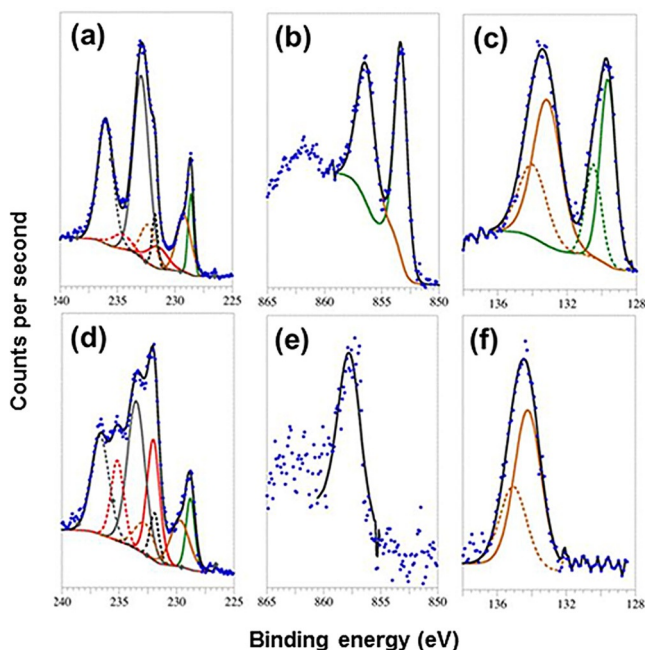


Figure 3. XPS spectra of (a) Mo3d from Mo₂C, (b) Ni2p from Ni₂P, (c) P2p from Ni₂P, (d) Mo3d from Ni₂P@Mo₂C, (e) Ni2p from Ni₂P@Mo₂C, and (f) P2p from Ni₂P@Mo₂C. All catalysts were annealed post-synthesis prior to XPS measurements and the data are normalized with respect to the C 1s peak set to 284.8 eV. Lines with the same color within a spectrum but solid and dotted are pairs of peak splitting for a bonding type.

and oxidized nickel species on the surface has been attributed to oxidation upon contact with air.^[27] The shift to higher binding energy for the oxidized phosphorus peak and the absence of peaks related to phosphide in the composite material is also consistent with previous observations on deposition of nickel phosphide on various supports such as alumina, silica, and nickel foam.^[28]

Electrochemical characterization

Electrocatalytic activities of the carbide, phosphide, and composite materials with various P/C ratios were measured in 0.5 M sulfuric acid (pH 0.30) and 0.1 M KOH (pH 13) by using a three-electrode rotating disc electrode. The electrolyte was saturated with a hydrogen flow prior to electrochemical measurements and was continuously purged during the measurements. All potentials are adjusted to the reversible hydrogen electrode (RHE). Current densities are calculated based on geometric surface area of the working electrode and the catalyst loading is 0.2 mg cm⁻². The onset potential is defined as the applied potential (vs. RHE) required to generate 10 mA cm⁻², unless otherwise stated.

The XRD plot in Figure 4a indicates that the Ni₅P₄ phase has emerged at 450 °C if hydrothermally synthesized Ni₂P (red) or Ni₂P supported on MWCNT (black) was annealed under argon. We chose 450 °C instead of 500 °C so that we could compare these results with previous reports on nickel phosphide electrocatalysts.^[12] Annealing Ni₂P in a reducing environment (5% H₂) increases the proportion of Ni₅P₄ (blue) in the nickel phosphide matrix.

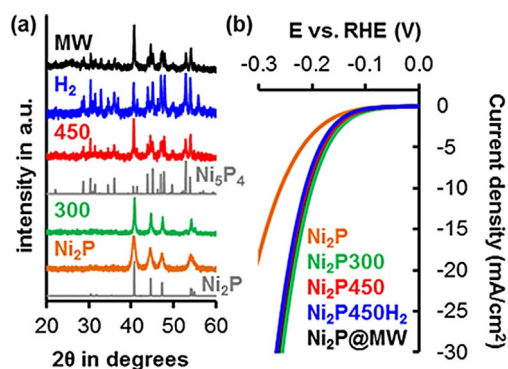


Figure 4. PXRD diffractograms (a) and corresponding HER polarization curves for Ni₂P annealed at various temperatures and under varying conditions (b). Numbers and H₂ after Ni₂P in (b) represent annealing temperatures in °C and annealing in 5% hydrogen in argon, respectively.

Ni₅P₄ has previously been reported to be a highly active electrocatalyst for HER in acid if synthesized utilizing a solvothermal synthesis method.^[29] Encapsulation in or supporting Ni₂P on high surface area carbon has also been shown to significantly improve the HER activities.^[30] However, Figure 4b indicates that the HER activities of hydrothermally derived Ni₂P remain unchanged irrespective of annealing conditions, support, or presence of Ni₅P₄. The initial improvement in HER activity upon annealing at 300 °C can be attributed to the removal of organic adsorbates on the catalyst surface as described previously for nickel phosphide synthesized by using trioctylphosphine.^[12] Unreacted phosphorus was volatilized at 450 °C during annealing in the tube furnace with simultaneous appearance of Ni₅P₄ if XRD patterns of the resulting powder were collected post-annealing.

However, supporting Ni₂P on Mo₂C improves the HER activities significantly in both acidic and basic electrolytes. As listed in Table 1, the HER overpotential generally decreases as the molar ratio of phosphide increases, under acidic electrolyte conditions. If the electrolyte is switched to 0.1 M KOH, the

Table 1. Electrochemical parameters in acid (A, pH 0.30) and base (B, pH 13) for catalysts annealed at 500 °C for 12 h under Ar flow at 0.5 L min⁻¹.

Cat ^[a]	ECSA [cm ²]		η_{10} vs. RHE [mV]		Tafel Slope [mV Dec ⁻¹]		Ex. Current [μ A cm ⁻²]	
	A	B	A	B	A	B	A	B
Mo ₂ C	37	27	192	225	60	56	6	2
0.16	42	18	231	272	69	58	4	1
0.37	41	21	239	265	82	66	13	2
0.76	32	19	212	238	75	60	16	1
1.89	35	13	196	237	67	62	18	2
4.69	22	13	196	246	72	72	12	6
9.76	14	9	190	269	88	71	69	3
18.8	8	4	184	321	90	84	57	2
Ni _x P _y	3	6	217	327	110	118	44	18
MW ^[b]	10	9	219	464	88	119	54	7
mix ^[c]	19	16	185	239	74	67	30	3

[a] Numbers represent Ni/Mo ratio. [b] Ni_xP_y deposited on multiwalled carbon nanotubes. [c] Physical mixture of phosphide and carbide in the same ratio as 1.89 catalysts.

onset potential becomes more positive up to the optimum Ni₂P loading of 1.89. At the highest Ni₂P loading (18.8), the HER activity is analogous to Ni_xP_y. The increase in Tafel slope and decrease in electrochemical surface area (ECSA; Figure S2 in the Supporting Information) at higher ratios can be attributed to the increased coverage of Mo₂C with Ni₂P to form interfacial sites and deposition of phosphide on high surface area MWCNT, respectively. Higher loadings of phosphide (> 1.89) result in mixed phases of nickel phosphide upon annealing, and the HER activity continues to improve in acid electrolyte. However, the activity starts to decrease beyond the optimum carbide phosphide ratio in base.

Despite a significant reduction in ECSA for Ni₂P@Mo₂C(9.76) and Ni₂P@Mo₂C(18.8), the increased HER activity in acid indicates either a higher density of active sites or higher turnover frequency (TOF) of the interfacial active sites.^[31] An increased Tafel slope to 120 mV/decade also indicates that the HER reaction rate is mostly determined by the reduction of hydronium ion on the catalyst surface through the Volmer step.^[32] The increase in overpotential of the composite catalyst at low phosphide ratios in comparison to Mo₂C can be attributed to the deposition of phosphorus on carbide active sites that cannot form phosphide–carbide interfaces. The P2p peak in the X-ray photoelectron spectroscopy (XPS) in Figure 3F indicates formation of phosphate on the surface. Thus, the analyte may be blocked from interacting with the active site by the surface phosphate species. At higher phosphide loading all the active sites on carbide must be converting to the interfacial sites and thus the overpotential is lower.

In the absence of an accurate insight into the nature and population of active sites on the surfaces, estimation of the catalytic properties such as turnover frequencies (TOF) of these materials cannot be quantified with precision. Instead, the Tafel slope and the associated exchange current densities can be used to infer the intrinsic catalytic properties of the materials.^[31] The higher exchange current in general for the catalysts in acidic media in comparison to alkaline media in Table 1, indicates enhanced comparative electrochemical interaction between the catalyst and the electrolyte at lower pH. The exchange current densities generally also increase in acid electrolyte with the increase in phosphide loading. The observations indicate that nanocrystalline phosphides may be better electrical conductors than the corresponding carbides and MWCNT.

Previous studies employed annealing in reducing environments to primarily remove the ligands adsorbed on the surface during the solvothermal decomposition method.^[12] On annealing of Mo₂C and the composite catalyst with optimized phosphide loading (1.89) under argon and in the presence of 5% H₂, the electrocatalytic activity of Mo₂C is analogous to that of nickel phosphide (Figure 4a). The activity of annealed Mo₂C improves in comparison to that of as-synthesized carbide, but remains unchanged irrespective of annealing under an inert or reducing environment (Figure S3a in the Supporting Information). Annealing the composite catalyst under a reducing environment leads to a lower HER overpotential in comparison to annealing under an inert atmosphere, as apparent from Figure S3b in the Supporting Information. Apparently, the passi-

vated carbide–phosphide interface leads to an improvement in electrocatalytic activity.

However, all the Ni₂P@Mo₂C catalysts annealed under H₂ contain two hexagonal phases (Figure S4) irrespective of phosphide to carbide ratio unlike in Figure 1b, where the Ni₅P₄ phase was observed only at higher ratios than 1.89 on annealing under inert argon atmosphere. The apparent improvement in overpotential could be a result of the emergence of the second phosphide phase, Ni₅P₄.

A comparison of HER activities of single-phase phosphide-deposited catalysts, that is, Ni₂P@Mo₂C and Ni₅P₄@Mo₂C, was not possible because hydrothermal synthesis could not be used to access the single-phase Ni₅P₄ nanomaterial on its own or deposited on Mo₂C. Previously, Laursen et al. reported that a solvothermal method can be utilized to synthesize phase-pure micron-sized Ni₅P₄ spheres, and the catalyst showed enhanced HER activities.^[29] The same investigation also reported that Ni₅P₄ converts to Ni₂P on annealing at temperatures above 350 °C. Based on the present evidence, the two phases seem to exist in dynamic equilibrium around 350 °C. Future endeavors may be worthwhile to identify a solvothermal method to obtain Ni₅P₄@Mo₂C and other composites of nickel phosphide on Mo₂C and so that their activities can be compared. In light of the evidence from Figure 4 and Figure S3 (in the Supporting Information), the observed enhancements in activities of the hydrothermally synthesized carbide–phosphide composite catalysts under investigation here are primarily attributed to the interfacial interaction between the two transition metal compounds.

The lowest overpotential (176 mV) to achieve 10 mA cm⁻² activity is afforded by annealing Ni₂P@Mo₂C(1.89) in a reducing environment (5% H₂). The overpotential to reach 40 mA cm⁻² HER activity can be improved by 100 mV if hydrothermally synthesized nickel phosphide is deposited on Mo₂C (Figure 5a). In addition, there is an improvement in the electrocatalytic stability of nickel phosphide if deposited on carbide, as depicted in Figure 5b. We employed Ni₂P@Mo₂C(0.76) for stability tests so that an identical initial applied potential could be used for both Ni_xP_y and Ni_xP_y@Mo₂C. The HER overpotential increased by 130 mV for Ni_xP_y within 18 h of constant potential electrolysis (CPE).

However, the corresponding increase in overpotential for Ni₂P@Mo₂C(0.76) is only 20 mV (Table S2 in the Supporting Information). The overpotential increases by 15 mV for Mo₂C within 18 h of CPE testing. The same composite catalyst showed remarkable electrochemical stability for 240 h if constant potential electrolysis (CPE) was conducted at 240 mV overpotential to generate 10 mA cm⁻² (Figure S5a in the Supporting Information). Comparison of the initial linear sweep voltammetry (LSV) curve with the one collected after 240 h showed an increase of 9 mV in overpotential (Figure S5b in the Supporting Information).

For comparison, a physical mixture of Ni_xP_y and Mo₂C was prepared by grinding annealed phosphide and carbide in the same molar ratio as optimized ratio (1.89). Although the significance of the Ni–Mo bimetallic catalyst is highlighted by the lower overpotential than Mo₂C and Ni_xP_y for the physical mix-

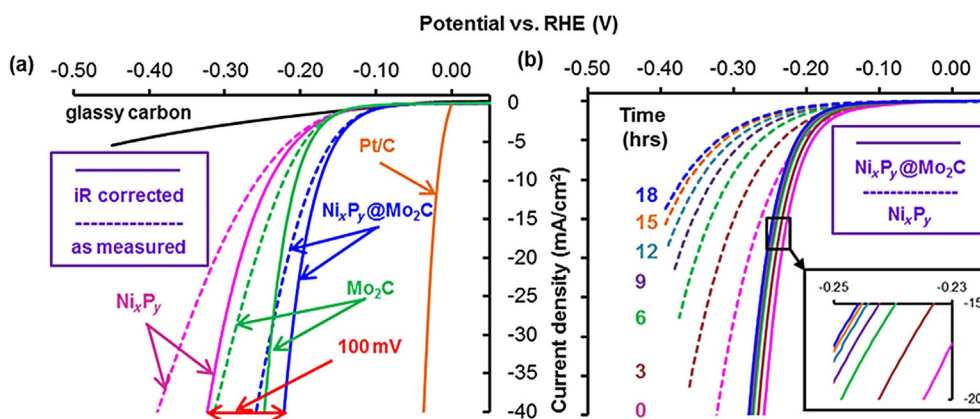


Figure 5. (a) *i*R corrected (solids) and as-obtained (dashed) HER polarization curves in 0.5 M H₂SO₄ for catalysts annealed at 450 °C for 12 h under 5% H₂ blended with Ar. The ICP-OES measured molar Ni₂P/Mo₂C ratio was 1.89 before annealing in H₂ environment. (b) Polarization curves for nickel phosphide (dashed) and nickel phosphide-deposited Mo₂C (solids) after constant potential electrolysis (CPE) to generate 10 mA cm⁻² for the stated hours. The Ni₂P/Mo₂C was 0.76 pre-annealing in H₂. The glassy carbon working electrode was rotated at 3500 rpm, Hg/HgSO₄ was the reference electrode and a gold wire as the counter electrode.

ture (mix) catalyst in Table 1, the extended stability can only be achieved if nickel phosphide is deposited and immobilized on carbide by hydrothermal incubation and high-temperature annealing. Rapid deactivation of hydrothermally synthesized unsupported Ni₂P in Figure 5b indicates that interaction with the support is crucial for the stability whereas bimetallic properties are critical for activity enhancement.

Conclusions

We have demonstrated that nickel phosphide can be preferentially deposited on molybdenum carbide by using a hydrothermal synthesis method. Emergence of a second phosphide phase, Ni₅P₄, upon annealing at 500 °C, indicates saturation of the carbide surface with phosphide. Unsupported phosphide and phosphide supported on carbon also shows a biphasic composition. The HER activity and stability of the carbide deposited with phosphide are superior to unsupported nickel phosphide. The enhancement in activity and stability is a result of the interfacial phosphide–carbide interaction. Our investigations demonstrate the utility of advanced carbide–phosphide composite materials for electrochemical energy conversion technologies.

Experimental Section

Safety statement

Synthesis routes for nickel phosphide and phosphide-deposited carbides utilized here require handling elemental red phosphorus under high temperature and pressure. Under such conditions, toxic and explosive phosphorus compounds can be released that are known to cause health and safety hazards. All personnel involved in such synthesis are advised to read safety documents obtained during the purchase of the chemicals and equipment. Hydrothermal reactors should be allowed to equilibrate to room temperature before opening inside a well-ventilated fume hood. Furnaces should also be allowed to equilibrate with the fume hood tem-

perature before unloading the annealing boats containing phosphides.

Materials

MoO₃, MWCNT (70–80% C), P (red), and NiCl₂·6H₂O were purchased from Sigma–Aldrich. Ethanol, methanol, HNO₃, and HCl were purchased from Fisher Scientific. HF and H₃BO₃ were purchased from Acros Organics. Stock solutions for ICP-OES of Ni (20 ppm), Mo (1000 ppm), and P (1000 ppm) were purchased from SPEX CertiPrep. Nafion solution (5 wt%, IonPower) and methanol (99.9% Sigma–Aldrich) were used for ink preparation for electrochemical half-cell experiments conducted in H₂SO₄ (99.9999% Alfa Aesar) and KOH (99.99% Sigma–Aldrich) diluted to 0.5 M and 0.1 M, respectively, with 18.2 MOhm cm water (Milli-Q). Ultrahigh purity nitrogen, hydrogen, and argon were obtained from Airgas. All the materials were used as purchased unless otherwise stated.

Catalyst synthesis

Mo₂C synthesis was modified from the carbothermic reduction method reported recently.^[11] A 20:1 ball to precursor mixture of MWCNT and MoO₃ was ball-milled at 300 rpm for 20 h to prepare a homogenous mixture. The mixture was placed on a quartz boat annealed in a tube furnace equipped with temperature control. The furnace ramped to 950 °C at 1 °C min⁻¹ under argon flow at 0.5 L min⁻¹. The furnace was allowed to cool down to room temperature naturally before collecting the powder and grinding, using an agate mortar and pestle. Ni₂P synthesis was performed as described by Deng et al.^[13] Various Ni₂P@Mo₂C catalysts were prepared as per the synthesis route for Ni₂P but with the addition of Mo₂C into the precursor mixture. Briefly, to obtain the 1.89 Ni₂P to Mo₂C ratio, NiCl₂·6H₂O (0.95 g) was added to deionized (DI) water (30 mL) and the solution stirred at 400 rpm for 10 min. Red P (0.70 g) was stirred in followed by Mo₂C (0.41 g), and the mixture stirred for an additional 20 min. Then, the slurry was transferred into a Teflon-lined hydrothermal bomb from Parr Instruments and heated to 140 °C for 12 h. After cooling to room temperature, the black suspension was washed by centrifugation at 4000 rpm with three 50 mL portions of DI water and one portion of anhydrous

ethanol. The supernatant was discarded and the residue was dried at 60 °C under vacuum for 6 h. The resulting powder was ground with a mortar and pestle and annealed in a tube furnace under argon or 5% H₂ in argon flow at 500 °C for 12 h to remove excess P. Ni₂P@MWCNT was also prepared by replacing Mo₂C with MWCNT and a physical mixture of Ni₂P and Mo₂C was obtained by grinding Mo₂C (0.41 g) and of Ni₂P (0.30 g) for 20 min.

Physical characterization

Powder X-ray diffraction (PXRD) patterns were collected with a Pan-analytical Empyrean diffractometer with CuK alpha1 source ($\lambda = 1.5406 \text{ \AA}$) with the voltage and current were 45 kV and 40 mA, respectively. Instrumental broadening for Scherrer analysis was determined by using a LaB₆ standard (660) from the National Institute of Standards and Technology (NIST). Scanning electron micrographs were collected with a Zeiss Dual Beam FIB/SEM instrument. TEM images were collected with a Zeiss Libra 200 HT FE MC instrument. XRD, TEM, and SEM were collected at the Joint Institute for Advanced Materials (JIAM) at the University of Tennessee, Knoxville. The transmission electron microscopy (TEM) associated with energy dispersive X-ray spectroscopy (EDX) analysis were performed with a FEI Tecnai Osiris 200 kV (S)TEM instrument equipped with EDX. All EDX analysis was conducted at the Vanderbilt Institute of Nanoscale Science and Engineering (VINSE). The TEM samples were prepared by sonicating the catalyst (1 mg) in methanol (5 mL) for 20 min and drop-casting 5 μL of the suspension on copper grids with formvar film on 400 square mesh.

XPS analyses were performed by using an Ulvac-PHI Versaprobe 5000. Monochromatic AlK _{α} X-rays (1486 eV), a 100 μm diameter X-ray spot, and a takeoff angle of 60° off sample normal were used in each acquisition. Pass energies of 187.7 eV and 23.5 eV were used for the survey and high-resolution acquisitions, respectively. Charge neutralization was accomplished by using 1.1 eV electrons and 10 eV Ar⁺ ions. The powder samples were pressed into a piece of indium foil and the foil was screwed onto a sample puck. Placing the -CH₂- type bonding in the carbon 1s spectrum at 284.8 eV corrected any minor energy shifts resulting from charging. Relative atomic concentrations were calculated by using peak areas and PHI handbook sensitivity factors.^[33]

Ion-coupled plasma optical emission spectroscopy (ICP-OES) measurements were performed with an Optima 7300 DV spectrometer from PerkinElmer. Catalysts were digested by using a microwave-assisted method prior to ICP-OES analysis analogous to one described previously.^[34] Briefly, the catalyst (1.0–2.0 mg) was suspended in a solution consisting of concentrated solutions of HCl (3 mL), HNO₃ (1 mL), and HF (0.2 mL). The mixture was incubated for 20 min at 1150 W by using a Multiwave 3000 microwave from Anton Parr. After digestion and cooling, H₃BO₃ (1 mL) was added and the concentration was brought to ICP-OES measurement range by diluting with 1 M HNO₃ before analysis.

Electrochemical characterization

A Pine Instruments rotating disk electrode (RDE) rotator, glassy carbon electrodes (0.1963 cm²), electrochemical cells, and a biologic VMP-3 potentiostat were used for all electrochemical measurements. A Radiometer Analytical XR-200 Hg/HgSO₄ (acid) or XR-400 Hg/HgO (base) reference electrode, and gold wire counter electrode were used. The reference electrode potentials versus RHE were determined by measuring the open circuit voltage (OCV) of a Pt electrode in hydrogen-saturated electrolyte. All procedures

and data described are reported against RHE. Catalyst inks were prepared by combining catalyst material (2.6 mg) with methanol (0.5 mL) and then adding 38 μL of Nafion for a 60:40 ratio of catalyst to Nafion. The inks were sonicated for at least 20 min. The required volume to achieve a catalyst loading of 200 $\mu\text{g cm}^{-2}$ was determined by depositing aliquots of the inks onto aluminum foil and weighing with a Mettler Toledo XP2U balance. The volume typically ranged between 8–12 μL . Glassy carbon (GC) electrodes were prepared by polishing with 5.0 micron then 0.05 micron alumina powders, rinsing, and sonicating in ultrapure water for 5 min and finally sonicated in 0.5 M H₂SO₄ for 5 min. The electrodes were cleaned electrochemically by scanning 10 CV cycles at 50 mVs⁻¹ between 0.1 and -0.8 V in nitrogen-saturated electrolyte. The background activity of the clean GCE electrodes was then measured by collecting 3 CVs between 0.1 and -0.8 V at a scan rate of 5 mVs⁻¹ in hydrogen-saturated electrolyte. Measurements were made while rotating the electrode at 3500 rpm to remove hydrogen bubbles. Afterward, the predetermined volume of catalyst ink was deposited onto the electrode. The catalyst testing was conducted in hydrogen-saturated electrolyte. The catalyst surface was first electrochemically cleaned in a similar manner to the bare GC electrode with the potential window selected to limit the current to 50 mAcm⁻² in acid and 20 mAcm⁻² in base. These ranges were selected because electrode delamination occurred at higher current densities. After cleaning, the hydrogen evolution activity was measured by collecting 5 CVs within the same potential window at a 5 mVs⁻¹ scan rate. Potentioelectrochemical impedance spectroscopy measurements were conducted at 0 V for each electrode to *iR* correct the data. The electrochemical surface area (ECSA) of the catalysts was determined by measurement of the double-layer capacitance (*C*_{DL}). These measurements were made by collecting CVs within the range 0–0.3 V (acid) and 0–0.4 V (base) at 100, 50, 20, 10, and 5 mVs⁻¹ scan rates. The fifth cycle was collected for the first three scan rates and the third cycle for the latter two to ensure stable values were selected. For most catalysts, no faradaic processes were observed within these regions. Within the regions where no faradaic processes are occurring, the current results from double layer capacitance according to the Equations (S1) and (S2) in the Supporting Information, where ν represents the scan rate and i_a and i_c are the cathodic and anodic currents, respectively. The double layer capacitance was determined by plotting the difference between i_a and i_c in the middle of the potential region versus the scan rate, where the slope is equal to twice the double layer capacitance. The ECSA is related to *C*_{DL} according to Equation (S4), where *C*_s is the area-specific capacitance of an atomically smooth electrode of the same material under the same conditions (e.g., temperature, electrolyte, concentration, etc.). As *C*_s is not available for these catalysts, we have chosen values of 30 $\mu\text{F cm}^{-2}$ for 0.5 M H₂SO₄ and 40 $\mu\text{F cm}^{-2}$ for KOH based on literature values of Ni and Mo electrodes.^[35] An example of the ECSA analysis is shown in Figure S6 in the Supporting Information for Mo₂C in acid. The Tafel slopes of each polarization curve were determined around the onset potentials according to the method described previously.^[11] The stability experiments were conducted for the catalysts by holding the electrode at -212 mV, the potential corresponding with a 10 mAcm⁻² current density for the Ni₂P@Mo₂C(0.76) and Ni₂P. After 3 or 8 h, a series of five polarization curves were collected at a 5 mVs⁻¹ scan rate. This process was repeated after each additional 3 or 8 h for a total hold CPE time.

Acknowledgments

This project was supported by Southeastern Sun Grant Center and the US Department of Transportation, Research and Innovative Technology Administration DTO559-07-G-00050. N.L. and S.C.C. also acknowledge the Southeastern Partnership for Integrated Biomass Supply Systems (IBSS), which is supported by AFRI 2011-68005-30410 from USDA NIFA. XRD was performed at the Joint Institute for Advanced Materials (JIAM) by using instruments that were procured through the DOE Nuclear Energy University Program (DE-NE0000693) 12-3528. STEM was performed at the Vanderbilt Institute for Nanoscience and Engineering (VINSE) by using an instrument procured using funds provided by the NSF (NSF EPS 1004083 TN-SCORE). The authors would also like to thank Ms. Choo Hamilton (CRC), Dr. John R. Dunlap, and Dr. Maulik Patel (JIAM) for assistance with ICP, SEM, TEM, and XRD.

Keywords: electrocatalysis • hydrogen evolution reaction • molybdenum carbide • nickel phosphide • water splitting

- [1] S. W. Boettcher, T. E. Mallouk, F. E. Osterloh, *J. Mater. Chem. A* **2016**, *4*, 2764–2765.
- [2] M. Zeng, Y. Li, *J. Mater. Chem. A* **2015**, *3*, 14942–14962.
- [3] C. C. McCrory, S. Jung, I. M. Ferrer, S. M. Chatman, J. C. Peters, T. F. Jaramillo, *J. Am. Chem. Soc.* **2015**, *137*, 4347–4357.
- [4] X. Zou, Y. Zhang, *Chem. Soc. Rev.* **2015**, *44*, 5148–5180.
- [5] X. Fan, Z. Peng, R. Ye, H. Zhou, X. Guo, *ACS Nano* **2015**, *9*, 7407–7418.
- [6] a) Y. N. Regmi, B. M. Leonard, *Chem. Mater.* **2014**, *26*, 2609–2616; b) A. M. Stux, C. Laberty-Robert, K. E. Swider-Lyons, *J. Solid State Chem.* **2008**, *181*, 2741–2747.
- [7] L. Z. Zeng, S. F. Zhao, W. S. Li, *Appl. Biochem. Biotechnol.* **2015**, *175*, 2637–2646.
- [8] a) X. Xu, F. Nosheen, X. Wang, *Chem. Mater.* **2016**, *28*, 6313–6320; b) K. Xiong, L. Li, L. Zhang, W. Ding, L. Peng, Y. Wang, S. Chen, S. Tan, Z. Wei, *J. Mater. Chem. A* **2015**, *3*, 1863–1867; c) S. Wang, J. Wang, M. Zhu, X. Bao, B. Xiao, D. Su, H. Li, Y. Wang, *J. Am. Chem. Soc.* **2015**, *137*, 15753–15759.
- [9] Y. N. Regmi, G. R. Waetzig, K. D. Duffee, S. M. Schmuecker, J. M. Thode, B. M. Leonard, *J. Mater. Chem. A* **2015**, *3*, 10085–10091.
- [10] C. Wan, Y. N. Regmi, B. M. Leonard, *Angew. Chem. Int. Ed.* **2014**, *53*, 6407–6410; *Angew. Chem.* **2014**, *126*, 6525–6528.
- [11] Y. N. Regmi, C. Wan, K. D. Duffee, B. M. Leonard, *ChemCatChem* **2015**, *7*, 3911–3915.
- [12] E. J. Popczun, J. R. McKone, C. G. Read, A. J. Biacchi, A. M. Wiltrout, N. S. Lewis, R. E. Schaak, *J. Am. Chem. Soc.* **2013**, *135*, 9267–9270.
- [13] Y. Deng, Y. Zhou, Y. Yao, J. Wang, *New J. Chem.* **2013**, *37*, 4083–4088.
- [14] a) D. Cai, B. Liu, D. Wang, Y. Liu, L. Wang, H. Li, Y. Wang, C. Wang, Q. Li, T. Wang, *Electrochim. Acta* **2014**, *115*, 358–363; b) W. Xiao, J. S. Chen, C. M. Li, R. Xu, X. W. Lou, *Chem. Mater.* **2010**, *22*, 746–754.
- [15] C. Tang, W. Wang, A. Sun, C. Qi, D. Zhang, Z. Wu, D. Wang, *ACS Catal.* **2015**, *5*, 6956–6963.
- [16] Y. Pan, Y. Liu, C. Liu, *J. Power Sources* **2015**, *285*, 169–177.
- [17] J. F. Callejas, C. G. Read, C. W. Roske, N. S. Lewis, R. E. Schaak, *Chem. Mater.* **2016**, *28*, 6017–6044.
- [18] F. Bachhuber, J. von Appen, R. Dronskowski, P. Schmidt, T. Nilges, A. Pfitzner, R. Wehrich, *Angew. Chem. Int. Ed.* **2014**, *53*, 11629–11633; *Angew. Chem.* **2014**, *126*, 11813–11817.
- [19] J. Kibsgaard, T. F. Jaramillo, *Angew. Chem. Int. Ed.* **2014**, *53*, 14433–14437; *Angew. Chem.* **2014**, *126*, 14661–14665.
- [20] N. Perret, X. Wang, L. Delannoy, C. Potvin, C. Louis, M. A. Keane, *J. Catal.* **2012**, *286*, 172–183.
- [21] M. D. Porosoff, X. Yang, J. A. Boscoboinik, J. G. Chen, *Angew. Chem. Int. Ed.* **2014**, *53*, 6705–6709; *Angew. Chem.* **2014**, *126*, 6823–6827.
- [22] A. P. Grosvenor, M. C. Biesinger, R. S. C. Smart, N. S. McIntyre, *Surf. Sci.* **2006**, *600*, 1771–1779.
- [23] a) I. Abu, K. Smith, *J. Catal.* **2006**, *241*, 356–366; b) Z. Yao, J. Tong, X. Qiao, J. Jiang, Y. Zhao, D. Liu, Y. Zhang, H. Wang, *Dalton Trans.* **2015**, *44*, 19383–19391; c) R. Franke, T. Chassé, P. Streubel, A. Meisel, *J. Electron Spectrosc. Relat. Phenom.* **1991**, *56*, 381–388.
- [24] L. S. Dake, *J. Vac. Sci. Technol. A* **1989**, *7*, 1634–1638.
- [25] W. Gruenert, A. Y. Stakheev, R. Feldhaus, K. Anders, E. S. Shpiro, K. M. Minachev, *J. Phys. Chem.* **1991**, *95*, 1323–1328.
- [26] Y. Li, C. Zhao, *Chem. Mater.* **2016**, *28*, 5659–5666.
- [27] T. Chen, D. Liu, W. Lu, K. Wang, G. Du, A. M. Asiri, X. Sun, *Anal. Chem.* **2016**, *88*, 7885–7889.
- [28] a) S. J. Sawhill, K. A. Layman, D. R. Van Wyk, M. H. Engelhard, C. Wang, M. E. Bussell, *J. Catal.* **2005**, *231*, 300–313; b) C. Tang, L. Xie, K. Wang, G. Du, A. M. Asiri, Y. Luo, X. Sun, *J. Mater. Chem. A* **2016**, *4*, 12407–12410.
- [29] A. B. Laursen, K. R. Patraju, M. J. Whitaker, M. Retuerto, T. Sarkar, N. Yao, K. V. Ramanujachary, M. Greenblatt, G. C. Dismukes, *Energy Environ. Sci.* **2015**, *8*, 1027–1034.
- [30] a) Y. Pan, W. Hu, D. Liu, Y. Liu, C. Liu, *J. Mater. Chem. A* **2015**, *3*, 13087–13094; b) P. Jiang, Q. Liu, X. Sun, *Nanoscale* **2014**, *6*, 13440–13445.
- [31] J. D. Benck, T. R. Hellstern, J. Kibsgaard, P. Chakthranont, T. F. Jaramillo, *ACS Catal.* **2014**, *4*, 3957–3971.
- [32] T. Shinagawa, A. T. Garcia-Esparza, K. Takanebe, *Sci. Rep.* **2015**, *5*, 13801–13822.
- [33] J. F. Moulder, W. F. S. P. E. Sobol, K. D. Bomben, *Handbook of X-Ray Photoelectron Spectroscopy*, Perkin-Elmer Corp., Eden Prairie, MN, **1995**.
- [34] P. Kim, A. Johnson, C. W. Edmunds, M. Radosevich, F. Vogt, T. G. Rials, N. Labbé, *Energy Fuels* **2011**, *25*, 4693–4703.
- [35] a) P. Gu, L. Bai, L. Gao, R. Brousseau, B. E. Conway, *Electrochim. Acta* **1992**, *37*, 2145–2154; b) W. A. Badawy, A. G. Gad-Allah, H. A. Abd El-Rahman, M. M. Abouromia, *Surf. Coat. Technol.* **1986**, *27*, 187–196; c) M. Turner, G. E. Thompson, P. A. Brook, *Corros. Sci.* **1973**, *13*, 985–991.

Manuscript received: November 18, 2016

Revised: December 13, 2016

Accepted Article published: December 15, 2016

Final Article published: February 14, 2017